High-frequency measurement of thin film superconducting hybrids for ultra-low dissipation information and quantum technology applications

Energy Transition Programme | Summer Research Report

Mohammed Mustafa Turkistani, Mentor: Dr Niladri Banerjee

Abstract

Thin-film superconducting hybrids are attractive for low-dissipation information processing and microwave quantum technologies because superconductors suppress dc resistive loss while magnetic and interfacial layers introduce tunable dynamical degrees of freedom. Their finite-frequency response is nevertheless not lossless: quasiparticles, vortex motion, magnetic damping and interface effects can all contribute to microwave absorption. This report combines nanoscale surface metrology with analysis of a supplied broadband microwave dataset to establish a materials-to-dynamics picture of Nb-based superconducting films and hybrids. Tapping-mode atomic force microscopy (AFM) was analysed for two thin-film systems. For the Nb/Au sample, three 10×10 μm regions gave a final processed mean areal RMS roughness $S_q = 0.499 \pm 0.067$ nm. For the newer Nb/Al_2O_3 sample, three 10×10 μm, 512×512 scans gave $S_q = 0.419 \pm 0.025$ nm and $S_a = 0.331 \pm 0.018$ nm after the documented corrections; the middle-centre image contained rare high protrusions, producing a peak-to-valley span of 13.95 nm and a kurtosis of 7.56 despite similar overall roughness. The supplied 2–20 GHz microwave dataset shows temperature- and field-dependent response for Nb, Nb/Au, NbN, Nb/Py and Nb/Al_2O_3 structures. In Nb(40 nm)/Au(3 nm), the upper critical field decreases from 1.90 T at 2.5 K to 0.62 T at 6.5 K, while a distinct spectral-drop field B^* tracks a lower field scale. For Nb(40 nm)/Al_2O_3(3 nm), the supplied transport fit gives $T_c = 8.408$ K, $B_{c2}(0) = 2.434$ T and $\xi(0) = 11.63$ nm. Ferromagnetic hybrids exhibit strong field-dispersive microwave branches whose geometry and temperature dependence are consistent with magnetic resonance in a superconducting environment. The principal outcome is an internally consistent baseline linking verified surface morphology, superconducting field scales and high-frequency spectral phenomenology while explicitly separating measured facts from unresolved physical mechanisms.

Date: 19 August 2026

Experimental microwave figures and numerical values reproduced from the host-group dataset supplied for this project; acquisition is not attributed to the student unless explicitly stated.

Contents

1 Introduction **2**

2 Related Work **3**

2.1 Type-II superconductivity and vortex electrodynamics . . . 3

2.2 Microwave-triggered vortex instabilities . . . 3

2.3 Ferromagnetic resonance and superconducting-ferromagnet hybrids . . . 4

2.4 AFM as surface metrology for superconducting thin films . . . 4

2.5 Research gap addressed by the present work . . . 4

3 Methodology **4**

3.1 AFM samples and acquisition . . . 5

3.2 AFM processing and quantitative metrics . . . 5

3.3 Broadband microwave measurement architecture . . . 6

3.4 Microwave samples and evaluation procedure . . . 6

4 Results **7**

4.1 Nb/Au AFM surface morphology . . . 7

4.2 Nb/Al_2O_3 AFM surface morphology . . . 8

4.3 Comparison of Nb/Au and Nb/Al_2O_3 AFM results . . . 10

4.4 Nb/Au broadband superconducting response . . . 11

4.5 Nb/Al_2O_3 superconducting microwave response . . . 12

4.6 Ferromagnetic hybrid response . . . 13

5 Discussion **14**

5.1 Surface quality and the significance of sub-nanometre roughness . . . 14

5.2 Superconducting microwave response and the B^* anomaly . . . 15

5.3 Magnetic hybrids and superconducting modification of resonance . . . 15

5.4 Implications for ultra-low dissipation and quantum technology . . . 15

6 Limitations and Future Work **16**

7 Conclusion **17**

References **17**

1 Introduction

Energy dissipation is a central constraint in modern information technology. Conventional charge-based electronics dissipate energy through resistive transport and repeated charging of circuit capacitances, while quantum information platforms impose even more stringent requirements because microwave loss directly limits coherence and measurement fidelity. Superconductors offer a fundamentally different electrodynamic regime: below their critical temperature T_c they support non-resistive dc current and strong magnetic screening. However, zero dc resistance does not imply zero loss at microwave frequencies. Thermally excited quasiparticles, moving magnetic vortices, dielectric or interface loss, and magnetic damping in hybrid structures can all absorb energy. Consequently, high-frequency characterisation is required to determine whether a candidate superconducting structure is genuinely low-loss under its intended operating conditions.

The project addressed this problem in Nb-based thin films and superconducting hybrids. The wider research programme at Imperial College London combines conventional superconducting films with normal-metal, insulating and ferromagnetic layers, with longer-term interest in reconfigurable magnetic systems and artificial spin ice. Such structures are scientifically interesting because several collective excitations may coexist. In a Type-II superconductor, magnetic flux penetrates as quantised vortices. Under an alternating current, pinned vortices can oscillate and, above a characteristic dynamical scale, move viscously and dissipate energy. In an adjacent ferromagnet, a transverse microwave magnetic field can excite coherent magnetisation precession and spin-wave modes. Superconducting screening, trapped flux, proximity effects and local magnetic stray fields can therefore alter the microwave response of the magnetic subsystem and vice versa [1–3].

A second requirement is structural quality. Thin-film electrodynamics depend on the continuity and uniformity of layers and interfaces. AFM does not measure superconductivity directly, but it provides a quantitative height field at nanometre-scale vertical resolution and is therefore useful for establishing whether the surface is smooth, whether morphology is consistent across the sample, and whether isolated protrusions or scanning artefacts are present before more advanced measurements are interpreted [4]. In this project, AFM was used to analyse Nb/Au and Nb/Al_2O_3 thin-film surfaces, with a documented Gwyddion processing workflow and quantitative areal roughness statistics.

The report also analyses a broadband microwave dataset supplied by the host group. The measurement platform uses a microwave source and coplanar waveguide (CPW), with the film placed face-down over the waveguide inside a cryostat and magnetic field. An RF diode and lock-in amplifier, together with a 490 Hz field modulation, detect a field-derivative microwave signal over frequencies between 2 and 20 GHz [5]. The dataset contains superconducting films, metal-capped superconductors, NbN, Nb/Py hybrids and insulating-spacer multilayers, measured in out-of-plane and in-plane magnetic-field geometries.

Note

Attribution of work. The AFM analysis, image processing and quantitative morphology reported here form the student's experimental analysis contribution. The broadband microwave maps and superconducting critical-field values were supplied by the host research group and are analysed here as project data; the report does not imply that the student independently operated the microwave/FMR apparatus.

The objectives of this report are therefore to: (i) establish the relevant superconductivity, vortex and magnetic-resonance physics; (ii) document a defensible AFM analysis for both Nb/Au and Nb/Al_2O_3 surfaces; (iii) analyse the field-, frequency- and temperature-dependent trends present in the supplied microwave dataset; (iv) compare the observations with established vortex-dynamics and superconducting-ferromagnet literature; and (v) identify which conclusions are supported by the present data and which mechanisms require further experiments.

2 Related Work

2.1 Type-II superconductivity and vortex electrodynamics

Superconductivity is characterised by a condensate with a phase-coherent macroscopic order parameter, vanishing dc resistance and the Meissner effect. Two characteristic length scales are particularly important. The coherence length ξ sets the scale over which the superconducting order parameter can recover from a local perturbation, whereas the London penetration depth λ sets the scale over which magnetic field is screened. Their ratio, $\kappa = \lambda/\xi$, distinguishes Type-I and Type-II behaviour; for $\kappa > 1/\sqrt{2}$, the material is Type II and supports a mixed state between lower and upper critical fields [6].

In the mixed state, magnetic flux enters in quantised vortices carrying the flux quantum

$$\Phi_0 = \frac{h}{2e} \approx 2.07 \times 10^{-15}\ \mathrm{Wb}, \tag{1}$$

where h is Planck's constant and e is the elementary charge. Each vortex contains a core of suppressed superconductivity and circulating supercurrent. Defects, thickness variations and magnetic stray fields can lower the local vortex energy and act as pinning sites. Vortex motion generates an electric field and is therefore a finite-frequency loss mechanism even when the dc superconducting state is intact.

The simplest radio-frequency model of a pinned vortex is the Gittleman–Rosenblum equation [7]

$$\eta \dot{u} + k_p u = \Phi_0 J_{\mathrm{rf}}, \tag{2}$$

where u is the vortex displacement, η is the viscous drag coefficient, k_p is the effective pinning stiffness and J_{rf} is the alternating current density. The characteristic depinning angular frequency is $\omega_p = k_p/\eta$. For $\omega \ll \omega_p$, the response is predominantly elastic and inductive; for $\omega \gg \omega_p$, viscous motion approaches the flux-flow regime and dissipation becomes stronger. This provides a direct physical reason for studying superconductors over a broad microwave-frequency range.

2.2 Microwave-triggered vortex instabilities

Nonlinear vortex motion may also generate abrupt spectral features. Awad *et al.* reported microwave-triggered flux avalanches in Pb films at low magnetic fields and low frequencies, with strong dependence on drive amplitude and the location of microwave excitation relative to the film edge [8]. That work is an important comparison for interpreting discontinuities in the present Nb/Au dataset, but similarity in appearance alone is not sufficient to assign the same mechanism. Field scale, temperature range, spatial dependence and drive-power dependence must all agree before such an interpretation is defensible.

2.3 Ferromagnetic resonance and superconducting-ferromagnet hybrids

For a ferromagnet, the macroscopic magnetisation $\mathbf{M}$ precesses around an effective magnetic field $\mathbf{H}_{\text{eff}}$. Its damped motion is described by the Landau–Lifshitz–Gilbert equation

$$\frac{d\mathbf{M}}{dt} = -\gamma\mu_0\mathbf{M}\times\mathbf{H}_{\text{eff}} + \frac{\alpha}{M_s}\mathbf{M}\times\frac{d\mathbf{M}}{dt}, \tag{3}$$

where γ is the gyromagnetic ratio, μ_0 the permeability of free space, α the dimensionless Gilbert damping constant and M_s the saturation magnetisation [9]. A transverse microwave field supplies the torque that drives the precession. At resonance, the microwave absorption is enhanced; the resonance position probes the effective magnetic fields, while linewidth contains information about damping and inhomogeneous broadening.

In thin films, demagnetising fields make the resonance strongly geometry-dependent. Superconducting layers introduce additional field redistribution and dynamic coupling. Jeon *et al.* found that the superconducting transition in thick $Nb/Ni_{80}Fe_{20}/Nb$ trilayers changes both resonance field and linewidth, with Meissner screening and trapped flux contributing to the magnetic dynamics [2]. Golovchanskiy *et al.* likewise reported strong FMR shifts in proximity-coupled superconductor–ferromagnet–superconductor multilayers [3]. These results motivate the in-plane Nb/Py and multilayer measurements in the supplied dataset.

2.4 AFM as surface metrology for superconducting thin films

AFM reconstructs surface topography by raster-scanning a sharp probe while monitoring the tip–sample interaction. In tapping mode, the cantilever oscillates near resonance and touches the surface intermittently, reducing the lateral force compared with contact mode [4]. The technique provides a quantitative height value at each pixel, enabling both visual morphology and statistical roughness analysis.

AFM data nevertheless require careful processing. Sample tilt, scanner bow, line-to-line offsets, transient feedback failures and periodic instrumental noise can dominate the apparent height variation. Plane levelling, row alignment and scar removal can correct identifiable artefacts, while Fourier filtering may suppress periodic spatial-frequency components. Such filtering must be disclosed because it can also remove real morphology and reduce the measured roughness. For that reason, the present analysis reports the exact processing sequence and compares pre-FFT and final filtered statistics for the newer Nb/Al_2O_3 scans.

2.5 Research gap addressed by the present work

The literature establishes the component physics—vortex pinning and depinning, FMR, superconducting screening and quantitative AFM—but it does not by itself determine the origin of a spectral branch in a specific sample. The practical gap is to combine sample-quality information with frequency-, field- and temperature-dependent microwave data while preserving the distinction between direct observations and model-based interpretation. The current report addresses that gap at an exploratory stage: it establishes robust morphology baselines for two Nb-based surfaces and uses the supplied broadband maps to identify superconducting boundaries, characteristic spectral field scales and magnetic-resonance branches without over-assigning their microscopic origin.

3 Methodology

3.1 AFM samples and acquisition

Two sets of AFM data were analysed. The first was a niobium–gold thin film referred to in project records as Nb7Au5. The exact deposition stack and substrate were not included in the supplied fabrication record, so the report uses the neutral label *Nb/Au* rather than treating the numerical filename as independently verified thickness metrology. Three representative tapping-mode scans were selected at upper-centre, middle-centre and lower-centre positions. Each scan covered 10×10 μm.

The second dataset was a niobium/aluminium-oxide sample stored under filenames containing "Nb7Al2O3-3". This naming is consistent with a nominal Nb/Al_2O_3 stack but, again, the exact layer thicknesses were not independently verified from a deposition log. The three scans covered 10×10 μm with 512×512 pixels, corresponding to a nominal lateral sampling interval of approximately 19.5 nm per pixel. They were acquired in tapping mode in the retrace direction at a scan rate of 0.629634 Hz, with a cantilever drive frequency close to 272.5 kHz. The middle-centre scan used somewhat different drive/setpoint amplitudes than the upper and lower scans, so very small differences between positions are not interpreted as intrinsic material changes.

3.2 AFM processing and quantitative metrics

Gwyddion was used for image processing. For the Nb/Au dataset, the final channels selected in the previous project analysis were produced by the following documented operations:

- Upper centre: Level → Remove Scars → Align Rows → FFT filter.
- Middle centre: Level → Align Rows → Remove Scars ×2 → FFT filter.
- Lower centre: Level ×2 → Align Rows → Remove Scars → FFT filter ×2.

For the newer Nb/Al_2O_3 Gwyddion files, the saved processing histories were: upper centre, level → align rows → 2D FFT filter; middle centre, level → remove scars → align rows → 2D FFT filter; and lower centre, level → align rows → remove scars → 2D FFT filter. Importantly, the channel named "Height" in these saved Gwyddion projects had already undergone the levelling/row-correction stage. It is therefore a *pre-FFT processed channel*, not an untouched raw instrument channel. A fully raw-to-final reconstruction would require the original NanoScope source files.

For an areal height field with N pixels of height z_i and mean height $\bar{z}$, the arithmetic mean roughness and RMS roughness were evaluated as

$$S_a = \frac{1}{N} \sum_{i=1}^{N} |z_i - \bar{z}| \,, \tag{4}$$

$$S_q = \sqrt{\frac{1}{N} \sum_{i=1}^{N} (z_i - \bar{z})^2}. \tag{5}$$

The total peak-to-valley span was defined as

$$S_z = z_{\max} - z_{\min}. \tag{6}$$

Skewness was used to quantify asymmetry of the height distribution and Pearson kurtosis to quantify the prominence of heavy tails and rare extremes. For a Gaussian height distribution, Pearson kurtosis is approximately 3. Reported ± values for AFM means are the standard deviation among the three measured positions; they are not instrument calibration uncertainties or confidence intervals.

3.3 Broadband microwave measurement architecture

The microwave dataset supplied by the host group used a CPW-based cryogenic measurement geometry [5]. The sample was placed film-side down on the CPW inside a cryostat and externally applied magnetic field. A microwave source drove the CPW. The transmitted/detected RF power was rectified using an RF diode, and a lock-in amplifier detected the response under a small magnetic-field modulation at 490 Hz. The resulting quantity is therefore a field-modulated derivative-type microwave signal rather than a direct calibrated surface resistance.

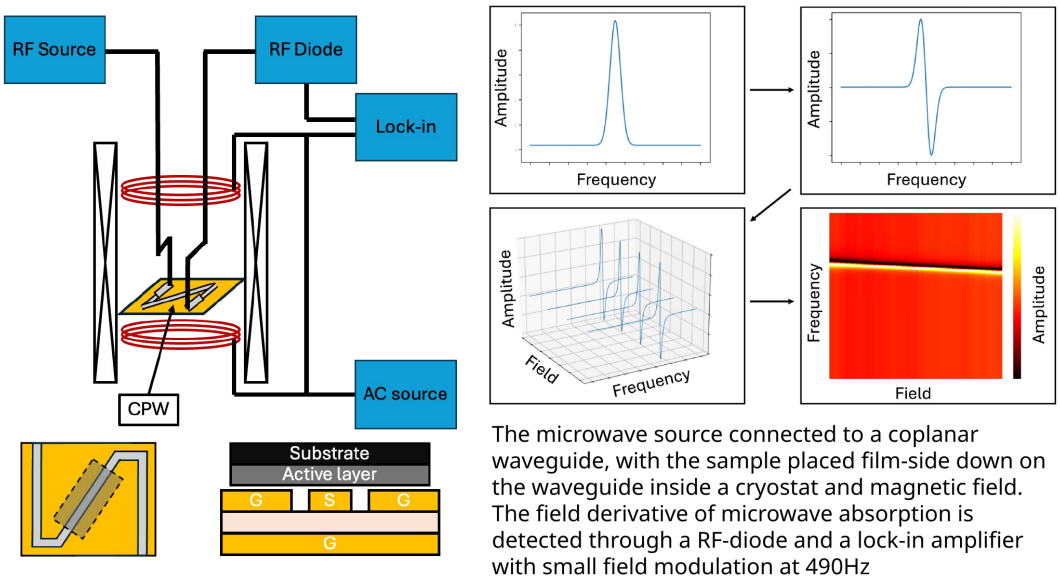


Figure 1 Measurement architecture supplied with the microwave dataset: RF excitation of a coplanar waveguide, film-side-down sample mounting in a cryogenic magnetic field, RF-diode detection and 490 Hz field-modulated lock-in readout. Figure reproduced from the supplied project presentation [5].

The frequency range in the supplied maps is generally 2–20 GHz. Out-of-plane (OOP) fields were used for superconducting films where perpendicular flux entry and vortex dynamics are central, while in-plane (IP) fields were used for several ferromagnetic hybrid measurements to resolve FMR-like dispersive branches. The data were inspected as frequency–field or frequency–temperature heatmaps. The present report extracts only quantities explicitly labelled in the supplied figures and does not infer absolute absorption, linewidth or microwave power where these were not provided.

3.4 Microwave samples and evaluation procedure

Table 1 summarises the sample labels and transition temperatures explicitly provided in the microwave presentation. Thicknesses are reported using the slide naming convention and should be regarded as nominal project labels.

Table 1 Selected samples and transition temperatures from the supplied microwave dataset [5].

Sample label	T_c (K)	Representative geometry
Nb40	7.517	OOP
Nb40/Au3	8.475	OOP
Nb15/Au5	6.522	OOP
Nb9/Au5	5.934	OOP
NbN37	12.39	OOP
NbN12.7	7.03	OOP
Nb40/Py30	7.016	OOP and IP
Nb100/Py30	8.260	OOP and IP
Nb40/$Al_2O_3$3	8.408	OOP
Nb40/Py3/Nb5	6.83	IP
Nb100/$Al_2O_3$3/Py20/$Al_2O_3$3/Nb100/Al2	6.83	IP

Evaluation focused on four questions: (1) whether the superconducting spectral boundary follows the expected reduction of B_{c2} with temperature; (2) whether additional field scales appear inside the superconducting state; (3) how IP magnetic-hybrid branches evolve with temperature and field; and (4) whether the observed phenomenology is consistent with, or clearly different from, specific mechanisms previously reported in the literature.

4 Results

4.1 Nb/Au AFM surface morphology

The earlier Nb/Au analysis found sub-nanometre areal RMS roughness at all three selected sample positions. The final processed values are listed in Table 2. The mean S_q is 0.499 ± 0.067 nm and the mean S_a is 0.390 ± 0.059 nm. The lower-centre region is the smoothest of the three by both S_a and S_q, but all positions remain below 0.55 nm RMS. The mean S_z of 6.94 ± 0.99 nm is much larger than S_q because S_z is controlled by only the most extreme minimum and maximum pixels.

Table 2 Nb/Au AFM roughness from the final processed channels selected in the previous project analysis.

Position	S_a (nm)	S_q (nm)	S_z (nm)
Upper centre	0.429	0.535	7.76
Middle centre	0.420	0.541	7.22
Lower centre	0.321	0.421	5.84
Mean ± SD	0.390 ± 0.059	0.499 ± 0.067	6.94 ± 0.99

Representative horizontal line profiles provided a second, local view of the same surface. Their RMS amplitudes were 0.360, 0.456 and 0.333 nm for upper, middle and lower centre, respectively, while profile peak-to-valley spans were 3.07, 2.92 and 2.15 nm. These profile statistics are not interchangeable with whole-image roughness because they sample only one line, but they confirm that the typical height fluctuation is on the sub-nanometre scale.

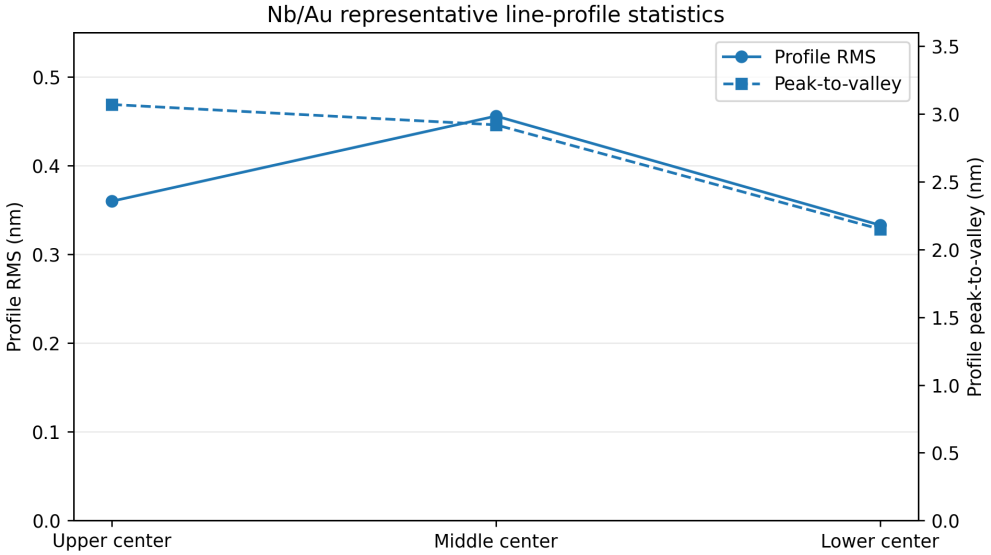


Figure 2 Summary statistics for the representative Nb/Au line profiles exported in the earlier AFM analysis.

4.2 Nb/Al_2O_3 AFM surface morphology

The newer Nb/Al_2O_3 dataset also exhibits sub-nanometre roughness after the documented corrections. Table 3 gives the statistics calculated directly from the final FFT-filtered height arrays. The three-position mean is $S_a = 0.331 \pm 0.018$ nm and $S_q = 0.419 \pm 0.025$ nm. The relative standard deviation of S_q is approximately 5.9%, indicating that the overall roughness is spatially consistent over the three measured regions.

Table 3 Final filtered Nb/Al_2O_3 AFM statistics calculated from the supplied Gwyddion data.

Position	S_a (nm)	S_q (nm)	S_z (nm)	Skewness	Kurtosis
Upper centre	0.334	0.418	6.014	0.091	3.142
Middle centre	0.348	0.444	13.948	0.437	7.564
Lower centre	0.312	0.395	7.704	0.088	3.474
Mean ± SD	0.331 ± 0.018	0.419 ± 0.025	—	—	—

The middle-centre scan has only slightly larger S_q than the other positions, but its S_z is nearly 14 nm. This is not evidence that the entire surface is 14 nm rough. The positive skewness and high kurtosis show that the distribution is dominated by a small number of unusually high pixels. The central 98% of the height distribution spans only about 2.07 nm in the middle region, comparable with about 1.93 nm for the upper and 1.87 nm for the lower region. The rare tall features therefore control the extreme-value statistic while leaving the RMS roughness relatively similar.

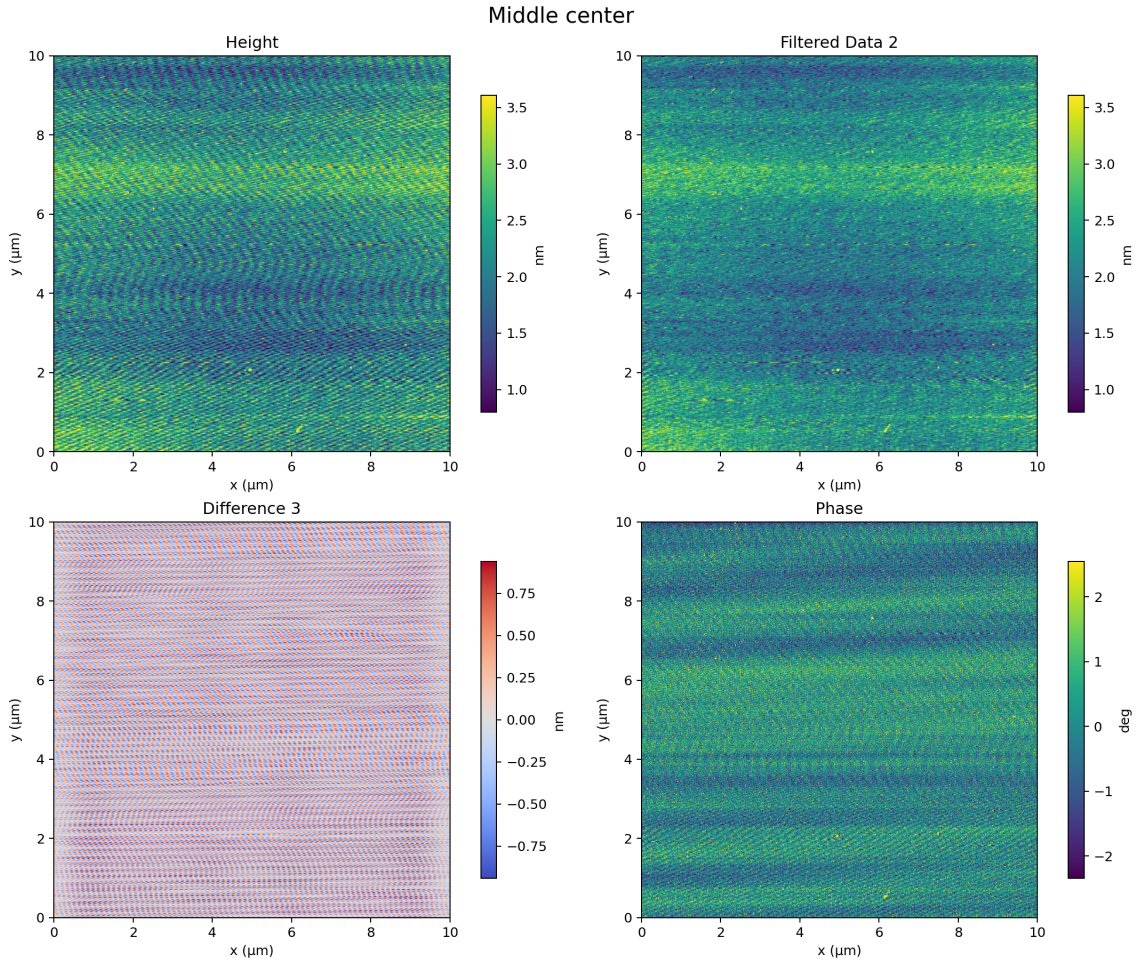
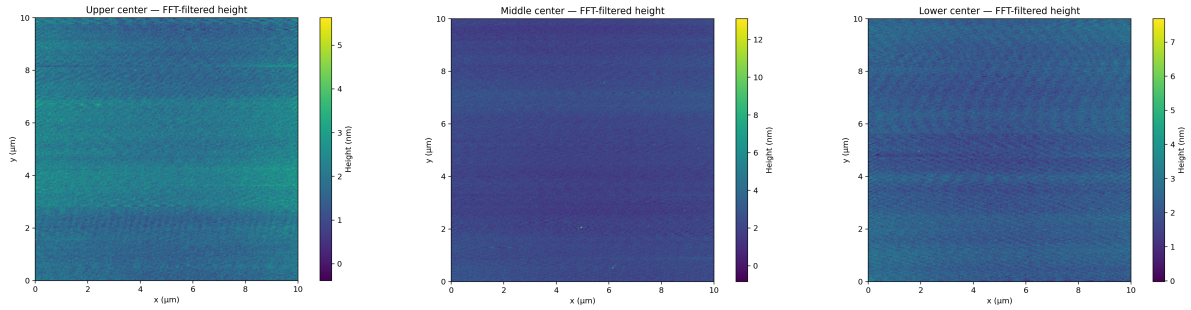


Figure 3 Middle-centre Nb/Al_2O_3 channels from the saved Gwyddion project. The pre-FFT "Height" channel contains a coherent diagonal periodic component; the final "Filtered Data 2" channel suppresses this component, while "Difference 3" explicitly shows what the FFT filter removed. The phase channel also contains related periodic structure.

The FFT correction is quantitatively significant. Before FFT filtering, the processed-height S_q values were 0.588, 0.597 and 0.571 nm for upper, middle and lower centre. The final values of 0.418, 0.444 and 0.395 nm correspond to reductions of approximately 28.9%, 25.6% and 30.9%, respectively. The RMS amplitude of the removed difference signal is approximately 0.40–0.41 nm in each scan. The highly regular diagonal structure of the difference map, together with a similar periodic component in phase, supports its interpretation as a scan/instrument contribution; nevertheless, because the correction removes substantial variance, all final roughness values are explicitly reported as *filtered* values.



(a) Upper centre (b) Middle centre (c) Lower centre

Figure 4 Final filtered topography for the three Nb/Al_2O_3 scan positions. Each image covers 10×10 μm.

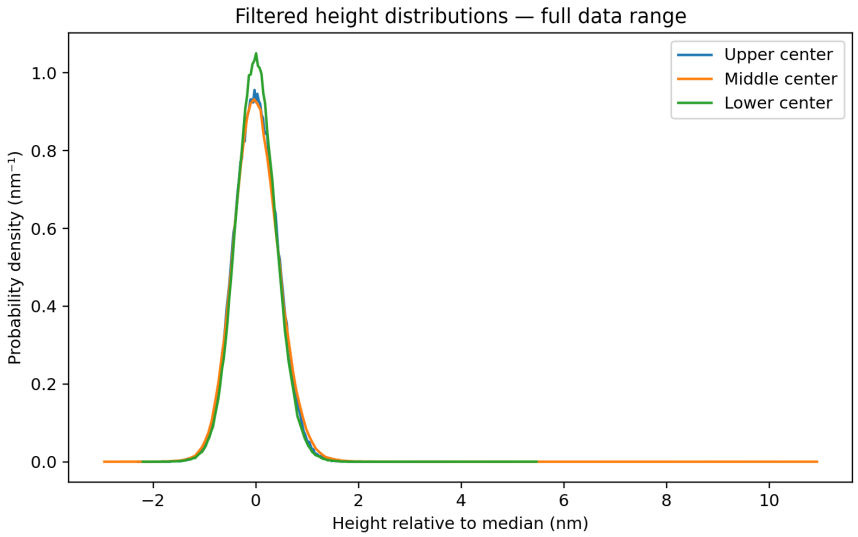


Figure 5 Full-range height distributions for the final filtered Nb/Al_2O_3 scans, plotted relative to each image median. The middle-centre distribution contains a stronger positive tail.

4.3 Comparison of Nb/Au and Nb/Al_2O_3 AFM results

Figure 6 compares the final processed S_a and S_q values. The mean S_q decreases from 0.499 nm for Nb/Au to 0.419 nm for the Nb/Al_2O_3 dataset, a numerical difference of 0.080 nm (about 16% relative to the Nb/Au mean). This should not be interpreted as proof that Al_2O_3 intrinsically produces a smoother Nb surface: the samples are different, their exact stacks are not independently verified here, and their processing histories are not identical. The robust conclusion is that both datasets show sub-nanometre RMS roughness across the selected 10×10 μm regions.

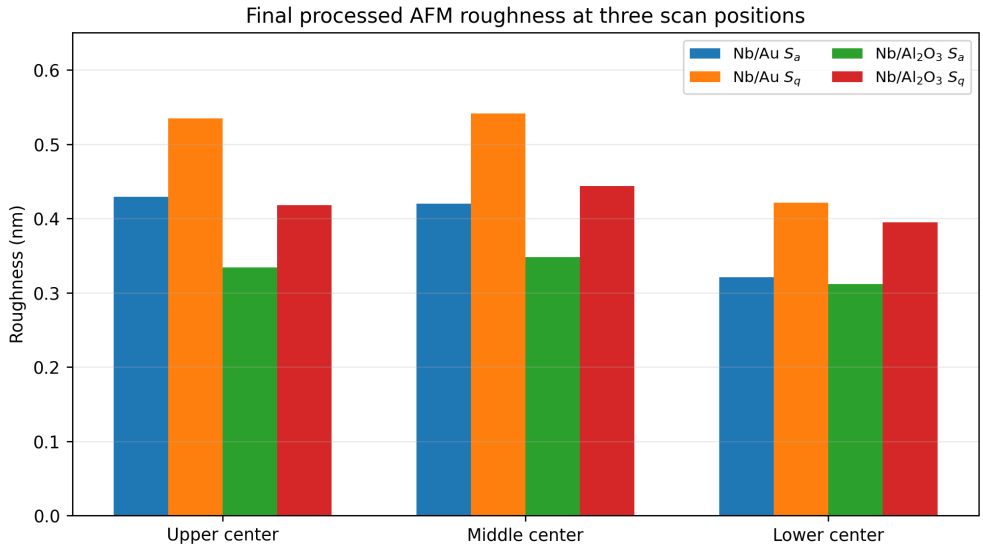


Figure 6 Final processed areal roughness for the Nb/Au and Nb/Al_2O_3 datasets. The comparison is descriptive rather than causal because the samples and processing histories differ.

4.4 Nb/Au broadband superconducting response

The supplied Nb(40 nm)/Au(3 nm) out-of-plane dataset shows a pronounced superconducting field boundary that contracts as temperature increases. The labelled upper critical fields are B_{c2} = 1.90 T at 2.5 K, 1.26 T at 4.5 K and 0.62 T at 6.5 K, consistent with progressive suppression of superconductivity as T approaches $T_c \approx 8.5$ K [5]. The frequency–temperature slices also show the superconducting spectral region shrinking toward the transition.

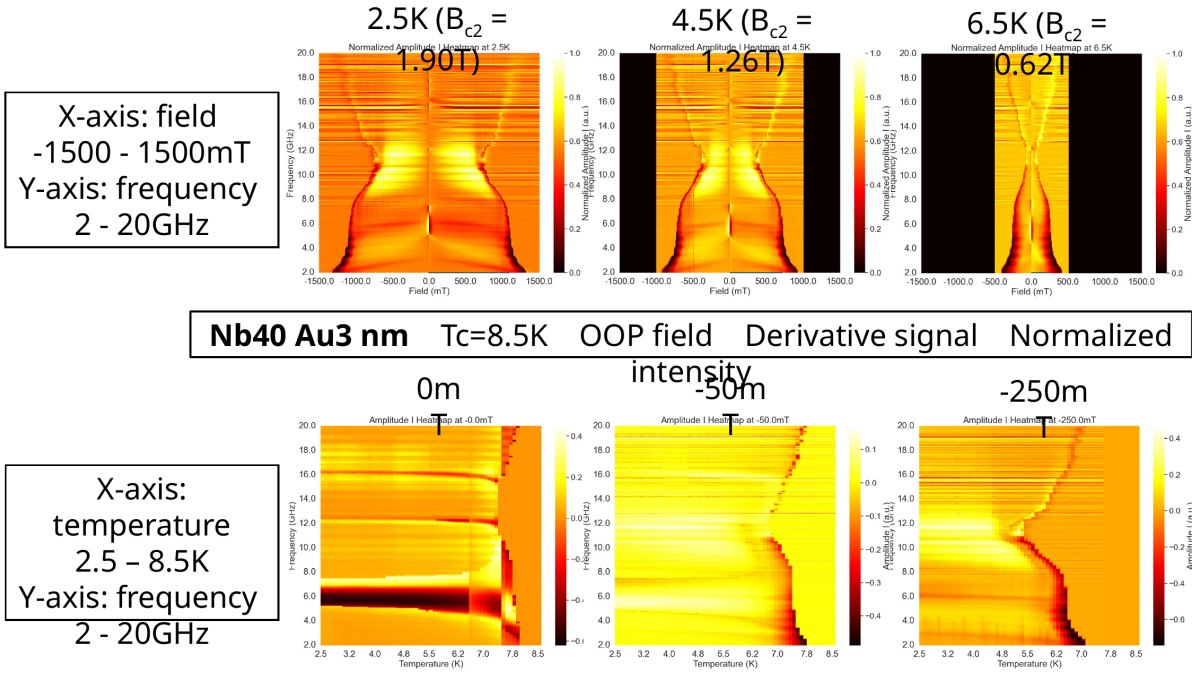


Figure 7 Supplied Nb(40 nm)/Au(3 nm) microwave maps. Top: frequency–field maps at 2.5, 4.5 and 6.5 K with labelled B_{c2} values. Bottom: frequency–temperature maps at selected applied fields. Reproduced from the supplied project dataset [5].

A second field scale, labelled B^* in the supplied analysis, marks a steep spectral-frequency drop inside the superconducting region. The extracted values are 1.108, 0.948, 0.726, 0.513, 0.256 and 0.039 T at 2.5, 3.5, 4.5, 5.5, 6.5 and 7.5 K, respectively. Over 2.5–5.5 K, B^*/B_{c2} remains approximately 0.54–0.60 before falling near T_c (Figure 8). The presentation compares this scale with the intervortex spacing $a_0(B)$ and coherence length $\xi(T)$ through the exploratory condition $a_0(B^*) = \gamma\xi(T)$. This is a useful phenomenological parameterisation but is not, by itself, a proof of the microscopic origin of B^*.

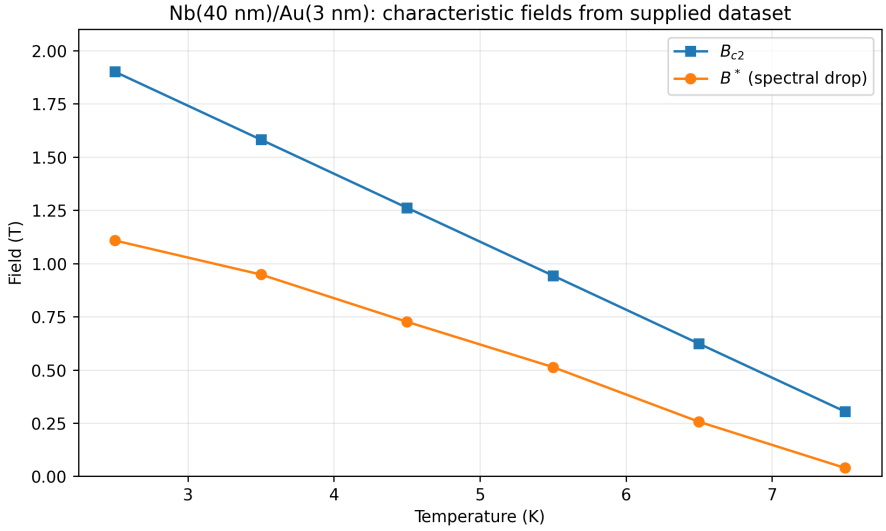


Figure 8 Upper critical field B_{c2} and the additional spectral-drop field B^* extracted from the supplied Nb(40 nm)/Au(3 nm) analysis.

The data were also compared with the microwave-triggered flux avalanches reported by Awad *et al.* [8]. Important differences argue against making a direct identification. The literature avalanches were reported at fields below approximately 20 mT and low frequency, were sensitive to the location of RF excitation and to a threshold drive, and occurred only below roughly $0.8T_c$. By contrast, the supplied Nb/Au anomaly extends to fields above 1 T at low temperature, spans the available 2–20 GHz window, was reported to remain similar when the film position relative to the CPW was changed, and persists toward approximately $0.9T_c$ [5]. Power-threshold data are not supplied. The most defensible conclusion is therefore that B^* is a reproducible spectral field scale whose microscopic mechanism remains unresolved.

4.5 Nb/Al_2O_3 superconducting microwave response

A separate microwave sample labelled Nb(40 nm)/Al_2O_3(3 nm) has $T_c = 8.408$ K in the supplied dataset. The out-of-plane map at 4.5 K shows a strong field-dependent boundary and internal frequency structure. A transport-derived $B_{c2}(T)$ fit using a 50% normal-resistance criterion gives $B_{c2}(0) = 2.434$ T and $\xi(0) = 11.63$ nm with $R^2 = 0.9995$ [5]. The coherence length is consistent with the standard Ginzburg–Landau relation

$$\xi(0) = \sqrt{\frac{\Phi_0}{2\pi B_{c2}(0)}}. \tag{7}$$

This microwave sample is *not assumed to be identical* to the AFM sample stored under the Nb7Al2O3-3 filename, so no direct roughness–B_{c2} correlation is claimed.

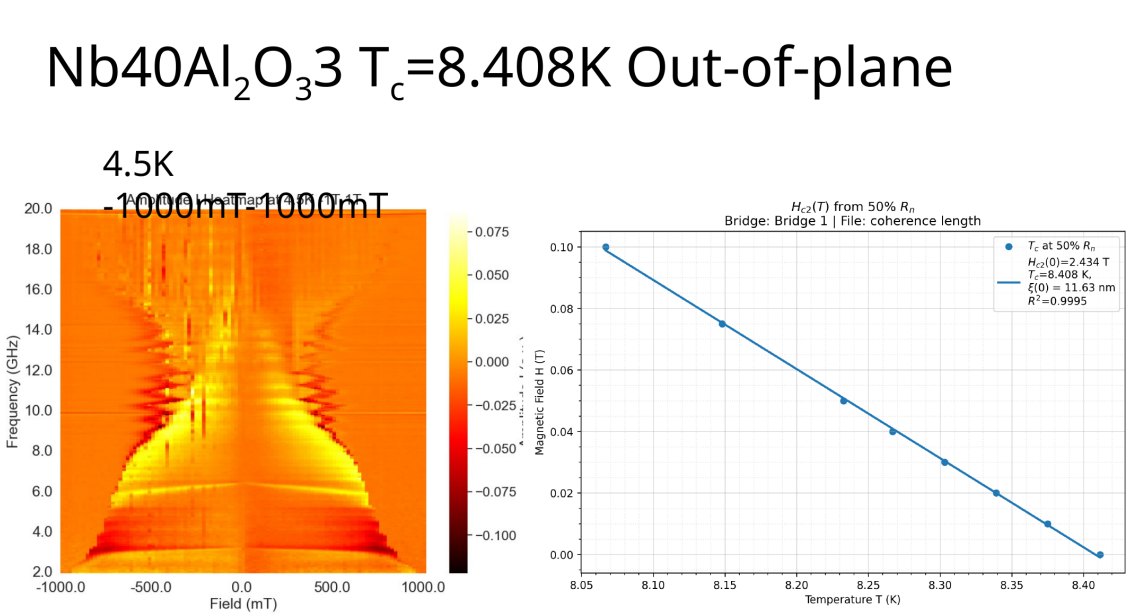


Figure 9 Supplied Nb(40 nm)/Al_2O_3(3 nm) out-of-plane microwave map at 4.5 K and the associated $B_{c2}(T)$ transport fit. The presentation reports T_c = 8.408 K, $B_{c2}(0)$ = 2.434 T, $\xi(0)$ = 11.63 nm and R^2 = 0.9995 [5].

4.6 Ferromagnetic hybrid response

The in-plane Nb40/Py30 dataset contains strong, approximately field-dispersive V-shaped branches extending across much of the 2–20 GHz window, together with weaker additional modes. Their curvature and temperature dependence change between 5.0, 5.5 and 6.0 K, demonstrating that the magnetic spectrum is not independent of temperature in the vicinity of the superconducting transition. The same project presentation contains related data for Nb100/Py30 and more complex Nb/Py/Nb and Nb/Al_2O_3/Py/Al_2O_3/Nb multilayers [5].

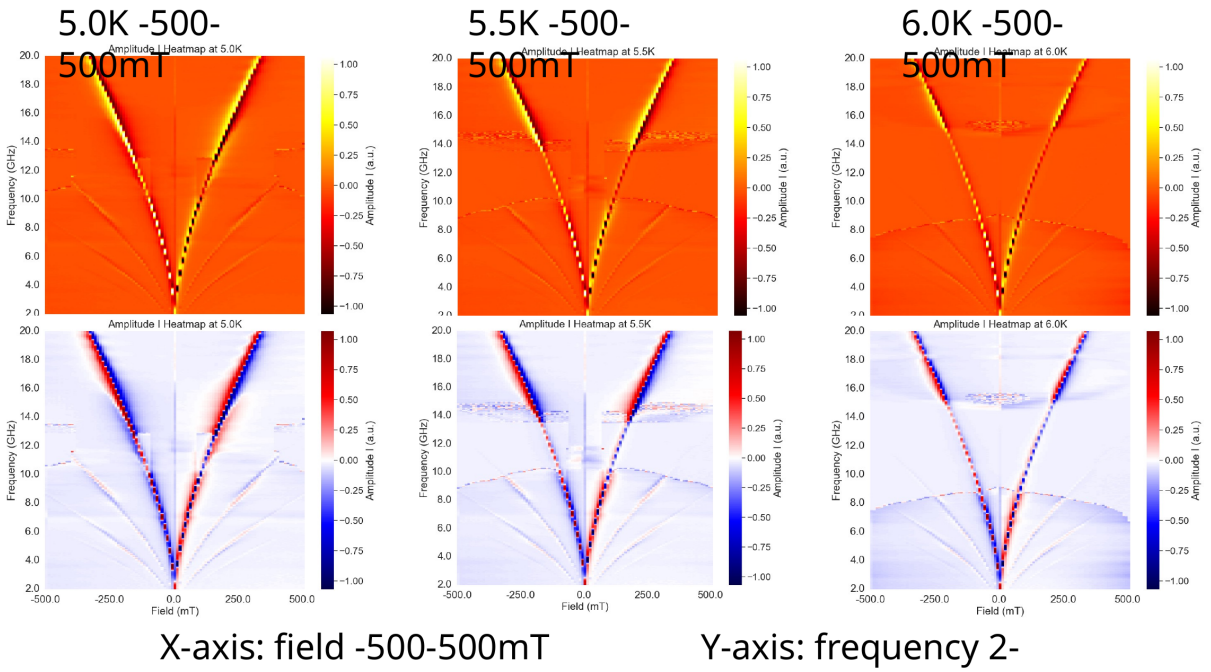


Figure 10 In-plane Nb40/Py30 frequency–field maps at 5.0, 5.5 and 6.0 K from the supplied microwave dataset. Strong dispersive resonance branches and additional weaker modes are evident. Reproduced from [5].

Without fitted resonance-field and linewidth datasets, the current report does not extract M_s, anisotropy fields or Gilbert damping. Nevertheless, the strong field dispersion and geometry dependence are qualitatively consistent with FMR/spin-wave dynamics, while the temperature evolution motivates a future quantitative comparison with superconducting-screening and proximity-coupling studies such as Refs. [2, 3].

5 Discussion

The AFM and microwave results probe different aspects of the same materials problem. AFM measures static surface topography; microwave spectroscopy probes dynamical electrical and magnetic response. The most important scientific discipline in combining them is to avoid treating correlation as causation. A smooth AFM surface is desirable for reproducible interfaces, but a value such as $S_q \approx 0.4$–0.5 nm does not by itself predict T_c, vortex depinning frequency, FMR linewidth or device quality factor.

5.1 Surface quality and the significance of sub-nanometre roughness

Both AFM datasets show sub-nanometre RMS roughness over the selected 10×10 μm regions. For Nb/Au, the final processed mean is 0.499 ± 0.067 nm; for the newer Nb/Al_2O_3 dataset it is 0.419 ± 0.025 nm. The small spatial spread in the latter suggests a reasonably uniform background morphology at the measured scale. The middle-centre image is a useful example of why multiple descriptors are needed: its RMS roughness is only about 0.444 nm, but rare tall features push S_z to 13.95 nm and kurtosis to 7.56. A single peak-to-valley number would therefore exaggerate the typical vertical fluctuation.

The FFT step requires particular caution. In the Nb/Al_2O_3 scans, it lowers S_q by 26–31% and removes a periodic component with an RMS amplitude around 0.4 nm. The difference map shows a coherent diagonal pattern rather than isolated surface objects, and similar periodicity appears

in phase, supporting an instrumental interpretation. Even so, a correction that removes nearly half of the pre-filter variance cannot be treated as cosmetic. For this reason, the report labels the headline numbers as *final filtered roughness*, gives the pre-FFT values, and identifies recovery of the original NanoScope files as an important validation step.

5.2 Superconducting microwave response and the B^* anomaly

The Nb40/Au3 maps show the expected contraction of the superconducting field range with increasing temperature, providing an internally consistent benchmark for the measurement. The additional B^* scale is more interesting because it occurs well below B_{c2} and roughly tracks a fixed fraction of B_{c2} over a substantial low-temperature interval. The supplied analysis relates this to the ratio between Abrikosov-lattice spacing and coherence length. That construction is physically motivated: both the intervortex distance and the vortex-core scale evolve as field and temperature change. However, many mechanisms can produce a spectral change inside the mixed state, including depinning crossovers, changes in collective vortex modes, nonuniform current distribution and instabilities. A length-scale coincidence alone is therefore insufficient for assignment.

Comparison with Awad *et al.* strengthens this conservative interpretation. The field scale and operating regime differ by orders of magnitude in field, while key signatures of the Pb-film avalanche mechanism—edge sensitivity and a verified microwave-power threshold—are absent or not yet tested in the supplied Nb/Au data. The correct conclusion is not that flux avalanches are impossible, but that the present evidence does not justify calling the observed high-field spectral drop the same phenomenon.

5.3 Magnetic hybrids and superconducting modification of resonance

The Nb/Py maps demonstrate why broadband measurement is essential in superconducting hybrids. A single fixed-frequency field sweep would reveal one or several peaks but would not expose the full mode dispersion. The two-dimensional maps show strong field-tunable branches and additional weaker modes whose behaviour changes with temperature. This is consistent with the general physics of a ferromagnetic thin film, where demagnetising fields, anisotropy and exchange determine the spectrum, and with prior superconducting-ferromagnet studies in which the transition into the superconducting state shifts or broadens magnetic resonances through Meissner screening, trapped flux and proximity coupling [2, 3].

The supplied figures are not sufficient for a unique mode assignment. In particular, quantitative separation of FMR, standing spin waves, CPW background resonances and superconductivity-induced features requires line-shape fits, field-symmetry tests, temperature sweeps across T_c and appropriate normal-state references. The present report therefore treats the branches as *FMR-like magnetic resonances* rather than claiming fitted magnetic parameters.

5.4 Implications for ultra-low dissipation and quantum technology

The project title connects the measurements to ultra-low dissipation and quantum technologies, but those terms should be interpreted as design motivations rather than demonstrated applications. The data show precisely why a superconducting film cannot be judged only by its dc resistance: the mixed state contains field- and frequency-dependent structure associated with vortex dynamics, while magnetic layers add resonant channels that can either be useful degrees of freedom or additional loss mechanisms. For microwave quantum circuits, trapped vortices and magnetic damping are generally undesirable unless they are intentionally engineered and coherently coupled. For unconventional information processing, by contrast, nonlinearity, memory and

reconfigurable resonances may be useful. The same material platform can therefore be promising only if its dynamical loss and control mechanisms are quantitatively understood.

6 Limitations and Future Work

The report is designed to be explicit about the present limits rather than hiding them behind the visual richness of the data.

1. **AFM spatial sampling is limited.** Three 10×10 μm regions were analysed for each surface. This is enough to compare selected positions but not to establish full-wafer uniformity. Future work should increase the number of regions and include at least one additional scan size at each position.
2. **The saved Nb/Al_2O_3 Gwyddion files do not contain a fully untouched raw height channel.** The channel called "Height" already contains levelling and row/scar corrections. The original NanoScope files should be re-opened and the full raw → levelled → row-corrected → FFT-filtered chain recalculated to quantify each operation independently.
3. **FFT filtering removes a substantial fraction of height variance.** Although the removed pattern is strongly periodic and likely instrumental, future scans should test this assignment experimentally by changing scan direction, scan rate and sample orientation. A real sample feature remains fixed to the specimen; a scan artefact generally follows the acquisition coordinates.
4. **Exact fabrication metadata are incomplete in the supplied AFM records.** The nominal filename conventions should be verified against deposition logs before linking surface statistics to a specific layer thickness or deposition condition.
5. **The microwave data are supplied processed maps rather than raw calibrated signals.** Absolute microwave power, RF field amplitude, detector calibration and raw traces are not provided in the presentation. Consequently, the report cannot extract an absolute surface resistance or energy-loss rate. Future analysis should retain raw lock-in traces and calibration data.
6. **The B^* mechanism is unresolved.** Power dependence, repeated field sweeps, spatial repositioning, ramp-rate dependence and magnetic-history dependence should be measured systematically. These tests can distinguish a linear depinning crossover from thermomagnetic instability or other nonlinear vortex processes.
7. **FMR parameters have not been fitted.** For the Nb/Py and multilayer samples, resonance fields should be extracted at each frequency and fitted with the appropriate in-plane or out-of-plane Kittel model. Linewidth as a function of frequency should then be used to separate Gilbert-like damping from frequency-independent inhomogeneous broadening.
8. **AFM and microwave measurements are not yet a one-to-one sample correlation.** The strongest future experiment would characterise the same physical specimen by AFM and microwave spectroscopy, with controlled variants of cap/spacer material and thickness. That would permit a real test of whether morphology or interface quality correlates with T_c, B_{c2}, depinning behaviour or magnetic linewidth.

The immediate next stage should therefore combine raw-data preservation, quantitative fitting and controlled sample series. For superconducting films, a Gittleman–Rosenblum-type analysis of the complex microwave response could extract a characteristic depinning frequency when amplitude and phase are available. For magnetic hybrids, Kittel and linewidth fits should be performed above and below T_c so that superconductivity-induced changes can be isolated

from normal-state temperature trends. The longer-term objective is to determine which hybrid architectures retain useful magnetic or vortex tunability while minimising irreversible microwave loss.

7 Conclusion

This project combined quantitative AFM surface analysis with high-frequency superconducting-hybrid data to establish a consistent picture of Nb-based thin films from morphology to microwave dynamics. The Nb/Au surface showed a final processed mean RMS roughness of $S_q = 0.499 \pm 0.067$ nm, while the newer Nb/Al_2O_3 dataset gave $S_q = 0.419 \pm 0.025$ nm and $S_a = 0.331 \pm 0.018$ nm across three 10×10 μm regions. The latter was spatially consistent in RMS roughness, although rare protrusions in the middle-centre image generated a much larger extreme height range. The analysis also demonstrated that FFT filtering removed a substantial periodic acquisition component, making explicit documentation of processing essential for scientifically meaningful roughness values.

The supplied 2–20 GHz microwave measurements showed clear temperature-dependent superconducting field boundaries and rich hybrid magnetic spectra. For Nb(40 nm)/Au(3 nm), B_{c2} decreased from 1.90 T at 2.5 K to 0.62 T at 6.5 K, while an additional spectral-drop field B^* tracked a lower field scale whose mechanism remains unresolved. For Nb(40 nm)/Al_2O_3(3 nm), the supplied analysis gave $T_c = 8.408$ K, $B_{c2}(0) = 2.434$ T and $\xi(0) = 11.63$ nm. Nb/Py and multilayer structures exhibited strong field-dispersive microwave branches that motivate quantitative FMR fitting across the superconducting transition. Taken together, the results support the central premise of the project: low dc resistance alone is not enough to qualify a superconducting hybrid for low-loss information or quantum technology. Surface quality, vortex dynamics, magnetic resonance and interface-dependent microwave response must be characterised together, with future work focused on raw-data calibration, power dependence, mode fitting and direct correlation on the same physical samples.

References

[1] Bill Qian. “Early Stage Assessment”. Internal research assessment, Imperial College London. 2025.

[2] Kun-Rok Jeon et al. “Effect of Meissner Screening and Trapped Magnetic Flux on Magnetization Dynamics in Thick Nb/Ni80Fe20/Nb Trilayers”. In: *Physical Review Applied* 11 (2019), p. 014061. DOI: 10.1103/PhysRevApplied.11.014061.

[3] I. A. Golovchanskiy et al. “Magnetization Dynamics in Proximity-Coupled Superconductor-Ferromagnet-Superconductor Multilayers”. In: *Physical Review Applied* 14 (2020), p. 024086. DOI: 10.1103/PhysRevApplied.14.024086.

[4] Bruker. *Atomic Force Microscopy for Materials*. 2017.

[5] Imperial College London superconducting devices and materials group. “MW data Nb 202607”. Internal project presentation and supplied microwave dataset. 2026.

[6] A. C. Rose-Innes and E. H. Rhoderick. *Introduction to Superconductivity*. 2nd revised. Pergamon Press, 1994.

[7] J. I. Gittleman and B. Rosenblum. “Radio-Frequency Resistance in the Mixed State for Subcritical Currents”. In: *Physical Review Letters* 16 (1966), pp. 734–736. DOI: 10.1103/PhysRevLett.16.734.

[8] A. A. Awad et al. “Flux avalanches triggered by microwave depinning of magnetic vortices in Pb superconducting films”. In: *Physical Review B* 84 (2011), p. 224511. DOI: 10.1103/PhysRevB.84.224511.

[9] J. M. D. Coey. *Magnetism and Magnetic Materials*. Cambridge University Press, 2010. DOI: 10.1017/CBO9780511845000.